# Modelling lidar-relevant optical properties of complex mineral dust aerosols

Josef Gasteiger, Matthias Wiegner, Silke Groß, Volker Freudenthaler, Carlos Toledano, Matthias Tesche & Konrad Kandler

# Modelling lidar-relevant optical properties of complex mineral dust aerosols

*By* JOSEF GASTEIGER[1], *, MATTHIAS WIEGNER[1], SILKE GROß[1], VOLKER FREUDENTHALER[1], CARLOS TOLEDANO[1,2], MATTHIAS TESCHE[3] and KONRAD KANDLER[4], [1]*Ludwig-Maximilians-Universität, Meteorologisches Institut, Theresienstr. 37, 80333 München, Germany;* [2]*Group of Atmospheric Optics, Valladolid University, Valladolid, Spain;* [3]*Leibniz-Institut für Troposphärenforschung, Permoserstr. 15, 04318 Leipzig, Germany;* [4]*Technische Universitiät Darmstadt, Institut für Angewandte Geowissenschaften, Schnittspahnstr. 9, 64287 Darmstadt, Germany*

## ABSTRACT

We model lidar-relevant optical properties of mineral dust aerosols and compare the modelling results with optical properties derived from lidar measurements during the SAMUM field campaigns. The Discrete Dipole Approximation is used for optical modelling of single particles. For modelling of ensemble properties, the desert aerosol type of the OPAC aerosol dataset is extended by mixtures of absorbing and non-absorbing irregularly shaped mineral dust particles. Absorbing and non-absorbing particles are mixed to mimic the natural mineralogical inhomogeneity of dust particles. A sensitivity study reveals that the mineralogical inhomogeneity is critical for the lidar ratio at short wavelengths; it has to be considered for agreement with the observed wavelength dependence of the lidar ratio. The amount of particles with low aspect ratios (about 1.4 and lower) affects the lidar ratio at any lidar wavelength; their amount has to be low for agreement with SAMUM observations. Irregularly shaped dust particles with typical refractive indices, in general, have higher linear depolarization ratios than corresponding spheroids, and improve the agreement with the observations.

## 1. Introduction

Mineral dust aerosols play an important role in the Earth's atmosphere; for example, they influence the radiative transfer and, as a consequence, they are relevant for the Earth's climate (e.g. Satheesha and Moorthy, 2005). Modelling the interaction of radiation with mineral dust aerosols is a challenging task (Kalashnikova and Sokolik, 2004; Nousiainen, 2009) because of the complexity of the microphysical particle properties (e.g., Kandler et al., 2009). Mineral dust aerosols consist of particles with a large variety of microphysical properties, that is, different sizes, shapes and composition. The mineralogical inhomogeneity, within single dust particles and from particle to particle, implies an inhomogeneity of the refractive index and the absorption properties. An adequate treatment of this aspect is crucial for assessing the radiative effects of mineral dust aerosols (Sokolik and Toon, 1999).

Active remote sensing by lidar systems is an important tool for aerosol research because it allows the vertically resolved detection of aerosols. Multichannel lidar systems allow the classification of aerosols and, to some extent, information about their microphysical properties can be extracted from the observations (e.g. Müller and Quenzel, 1985; Müller et al., 1999; Böckmann and Wauer, 2001; Veselovskii et al., 2010; Gasteiger et al., 2011; Osterloh et al., 2011). For that extraction, the relationship between microphysical and optical properties has to be known from numerical simulations. Because of the complexity of the microphysical properties, assumptions are usually applied for such simulations. The optical properties, however, may be sensitive to these assumptions and, as a consequence, the interpretation of remote sensing measurements may become biased in the worst case. Therefore, the investigation of the effect of these assumptions is essential for improvements in the interpretation of remote sensing measurements.

The SAMUM field campaigns in Morocco (2006, SAMUM-1) and Cape Verde (2008, SAMUM-2) provide a comprehensive basis for the investigation of many aspects of mineral dust aerosols because an extensive set of physical and optical dust properties was derived using numerous measurement

techniques (Heintzenberg, 2009; Ansmann et al., 2011). In Wiegner et al. (2009) we modelled lidar-relevant optical properties of mineral dust aerosols using information about the microphysical aerosol properties derived from in situ measurements and electron microscopy during SAMUM-1. For optical modelling, we assumed homogeneous mixtures of dust spheroids. The comparison with optical properties derived from corresponding lidar measurements showed agreement of some parameters, but the spectral dependency of the lidar-relevant optical properties were not satisfactorily captured by optical modelling.

In this paper, we extend the study of Wiegner et al. (2009) by modelling of irregularly shaped particles. We consider the mineralogical inhomogeneity of natural mineral dust aerosols by modelling mixtures of absorbing and non-absorbing dust particles. Therefore, we first describe the methods that we use for modelling of optical properties (Section 2). In the next step, we investigate the optical properties of single dust particles (Section 3). After that, optical properties of mineral dust ensembles are modelled, and the sensitivity to changes of their microphysical properties is discussed (Section 4). Finally, the modelled optical properties are compared with optical properties derived from lidar measurements during the SAMUM-1 and SAMUM-2 field campaigns (Section 5).

## 2. Modelling optical particle properties

In this section, we define relevant properties of single aerosol particles and aerosol ensembles, and describe the methods that we use for modelling the optical properties of non-spherical particles.

### 2.1. Definition of aerosol properties

We assume that aerosol particles are homogeneous, that is, each particle consists of only a single material. Furthermore, we assume that particles are randomly oriented. This is a widely used assumption for aerosols; we know only of one case where partial particle alignment was observed (Ulanowski et al., 2007).

The physical properties of a homogeneous randomly oriented particle that are relevant for its optical properties at a given wavelength are the shape, the size and the refractive index $m$. In case of a non-spherical particle, different definitions for its size are available. Throughout this paper, unless otherwise noted, we use the radius of a sphere with equal geometric cross section

$$r_{\mathrm{c}} = \sqrt{\frac{C_{\mathrm{geo}}}{\pi}}. \tag{1}$$

$C_{\mathrm{geo}}$ is the orientation-averaged geometrical cross-sectional area of the particle. We use $r_{\mathrm{c}}$ for the specification of particle size because $C_{\mathrm{geo}}$ is the primary parameter for the extinction of light by a particle larger than the light wavelength (van de Hulst, 1981). Another commonly used description for the size of a

non-spherical particle is the volume-equivalent radius

$$r_{\mathrm{v}} = \sqrt[3]{\frac{3V}{4\pi}}, \tag{2}$$

where $V$ is the volume of the particle. The ratio between volume-equivalent radius $r_{\mathrm{v}}$ and cross-section-equivalent radius $r_{\mathrm{c}}$ is given by

$$\xi_{\mathrm{vc}} = \frac{r_{\mathrm{v}}}{r_{\mathrm{c}}} = \sqrt{\frac{3\sqrt{\pi}}{4}} \frac{\sqrt[3]{V}}{\sqrt{C_{\mathrm{geo}}}}. \tag{3}$$

For a non-spherical particle, $r_{\mathrm{v}}$ is smaller than $r_{\mathrm{c}}$, thus $\xi_{\mathrm{vc}}$ is smaller than 1. $\xi_{\mathrm{vc}}$ is equal to 1 in case of spheres. The size parameter $x$ of a particle at a given wavelength $\lambda$ is defined as

$$x = \frac{2\pi r}{\lambda}. \tag{4}$$

As we use $r = r_{\mathrm{c}}$, the size parameter $x$ is also specified in terms of cross-section-equivalent spheres, unless otherwise noted in this paper.

We describe the size distribution $n(r)$ of the particles in an aerosol ensemble by log-normal distributions (Hess et al., 1998):

$$n(r) = \frac{\mathrm{d}N}{\mathrm{d}r} = \frac{N_0}{\sqrt{2\pi}\,\ln\sigma\,r} \exp\left[-\left(\frac{\ln r - \ln r_0}{\sqrt{2}\ln\sigma}\right)^2\right]. \tag{5}$$

$n(r)$ is the particle number density per radius interval, $N_0$ the total number density of the particles, $r_0$ is the modal radius and $\sigma$ is a parameter for the width of the size distribution.

The optical properties of randomly oriented aerosol particles at a given wavelength $\lambda$ are specified by the extinction cross section $C_{\mathrm{ext}}$, the scattering cross section $C_{\mathrm{sca}}$ and the scattering matrix $\mathbf{F}(\theta)$, which depends on the scattering angle $\theta$. The single scattering albedo is given by $\omega_0 = C_{\mathrm{sca}}/C_{\mathrm{ext}}$. Normalization of the cross sections $C_{\mathrm{ext}}$ and $C_{\mathrm{sca}}$ by $C_{\mathrm{geo}}$ results in the extinction efficiency $q_{\mathrm{ext}}$ and the scattering efficiency $q_{\mathrm{sca}}$.

The extinction coefficient $\alpha$ of an aerosol ensemble at a given wavelength $\lambda$ can be calculated by

$$\alpha = \int_{r_{\mathrm{min}}}^{r_{\mathrm{max}}} C_{\mathrm{ext}}(r)\, n(r)\, \mathrm{d}r. \tag{6}$$

This equation is for integration over the size distribution and fixed particle shape and refractive index $m$. The integration range from $r_{\mathrm{min}}$ to $r_{\mathrm{max}}$ (integration limits omitted hereafter) should cover all particle radii that contribute to light extinction. The backscatter coefficient $\beta$ is calculated by

$$\beta = \int C_{\mathrm{sca}}(r)\, \frac{F_{11}(r, 180°)}{4\pi}\, n(r)\, \mathrm{d}r. \tag{7}$$

$F_{11}$ is the (1,1)-element of the scattering matrix; it is also known as the phase function and its integral over all solid angles is $4\pi$. By using the lidar ratio

$$S(r) = 4\pi\, \frac{C_{\mathrm{ext}}(r)}{C_{\mathrm{sca}}(r)\, F_{11}(r, 180°)} \tag{8}$$

which relates extinction to backscattering, the backscatter coefficient can be expressed by

$$\beta = \int C_{\text{ext}}(r) \, \frac{1}{S(r)} \, n(r) \, dr. \tag{9}$$

The lidar ratio of an aerosol ensemble is

$$S = \frac{\alpha}{\beta}. \tag{10}$$

The linear depolarization ratio of an ensemble is calculated by

$$\delta_{\text{l}} = \frac{\int C_{\text{ext}}(r) \, \frac{1}{S(r)} \quad d(r)/2 \quad n(r) \, dr}{\int C_{\text{ext}}(r) \, \frac{1}{S(r)} \, (1 - d(r)/2) \, n(r) \, dr} \tag{11}$$

with the depolarization parameter (Gimmestad, 2008)

$$d(r) = 1 - \frac{F_{22}(r, 180°)}{F_{11}(r, 180°)}. \tag{12}$$

For a given depolarization parameter, the linear depolarization ratio is calculated by

$$\delta_{\text{l}} = \frac{d/2}{1 - d/2}. \tag{13}$$

The Ångström exponent for extinction

$$\kappa_{\text{ext}} = \frac{\ln \alpha(\lambda_1) - \ln \alpha(\lambda_2)}{\ln \lambda_2 - \ln \lambda_1} \tag{14}$$

is used for the characterization of the wavelength dependence of the extinction in the wavelength range from $\lambda_1$ to $\lambda_2$. Analogously to $\kappa_{\text{ext}}$, an Ångström exponent for backscatter can be defined as

$$\kappa_{\text{bsc}} = \frac{\ln \beta(\lambda_1) - \ln \beta(\lambda_2)}{\ln \lambda_2 - \ln \lambda_1}. \tag{15}$$

The optical properties of mixtures of different shapes and refractive indices $m$ are calculated by adding the size-integrated extensive properties (eq. 6, eq. 9 or numerator and denominator of eq. 11) of each particle shape and refractive index $m$ (Gasteiger et al., 2011).

## 2.2. Optical modelling of irregularly shaped particles

Optical properties of particles with six irregular shapes are modelled. These shapes are shown in Fig. 1 . Shapes A, B and C are prolate spheroids with surface deformations according to the Gardner series (Gardner, 1984). Their aspect ratios $\epsilon'$ are 1.4, 1.8 and 2.4, respectively. Shape D is an aggregate particle, consisting of overlapping ellipsoids, again with surface deformations according to the Gardner series. The spheroid equivalent of shape D is a prolate spheroid with $\epsilon' \approx 1.8$. Shapes E and F have flat surfaces and edges. The spheroid equivalent of shape E is an oblate spheroid with $\epsilon' \approx 1.3$; the deviation of shape E from spherical shape is smaller than for the other shapes. Shape F is derived from shape E by stretching the particle by a factor
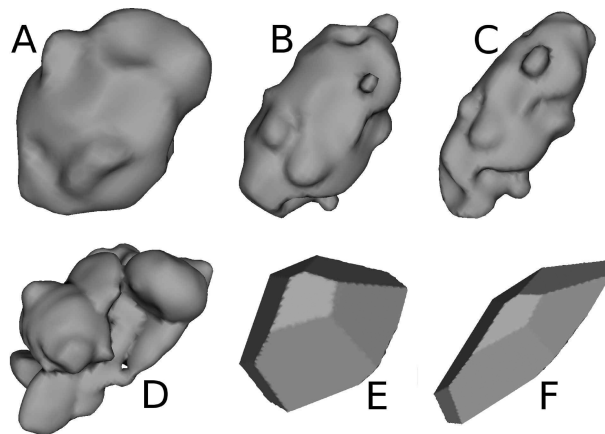


Fig 1. Irregularly shaped particles for model calculations.

of 2 in one dimension, and it may be approximated by a prolate spheroid with $\epsilon' \approx 2.3$.

These shapes are created using the volume modelling language Hyperfun (Valery et al., 1999). We use ADDA (Yurkin et al., 2007) for optical modelling of these particles. ADDA is an implementation of the Discrete Dipole Approximation (DDA); we use the DDA formulation 'filtered coupled dipoles' (Piller and Martin, 1998; Yurkin et al., 2010), which is included in ADDA. For size parameters $x \geq 10$, the particles are described by 11 dipoles per wavelength. For $x < 10$ the same particle description as for $x = 10$ is used, thus the number of dipoles per wavelength increases with decreasing $x$. The stopping criterion for the iterative solver of ADDA is set to $10^{-3}$.

To facilitate fast modelling of the optical properties of aerosol ensembles, we store the optical properties of a large number of different single aerosol particles in a database. The database contains all relevant optical parameters, that is, the scattering matrix $\mathbf{F}(\theta)$, the extinction efficiency $q_{\text{ext}}$ and the scattering efficiency $q_{\text{sca}}$, for six irregular shapes (Fig. 1), for four real parts of the refractive index $m_{\text{r}}$ (1.48, 1.52, 1.56 and 1.60), for six imaginary parts $m_{\text{i}}$ (0, 0.00215, 0.0043, 0.0086, 0.0172 and 0.0344), and for 37 volume-equivalent size parameters $x_{\text{v}}$ up to 20.8 (step width $+0.2$ for $x_{\text{v}} \leq 2.0$, and logarithmically equidistant steps of factor $\approx 1.1$ for $x_{\text{v}} \geq 2.0$). An upper limit for the size parameter is necessary because the computation time of the Discrete Dipole Approximation rapidly increases with increasing size parameter $x$.

For each particle shape, the factor $\xi_{\text{vc}}$ for the conversion between volume-equivalent radius $r_{\text{v}}$ and cross-section-equivalent radius $r_{\text{c}}$ is calculated. Knowledge about $\xi_{\text{vc}}$ is necessary because cross-section-equivalent radii are used in the subsequent sections whereas the ADDA calculations were conducted for volume-equivalent radii. According to eq. (3), $C_{\text{geo}}$ has to be known for the calculation of $\xi_{\text{vc}}$; we calculate $C_{\text{geo}}$ by averaging numerically evaluated particle cross sections at many different particle orientations. We find $\xi_{\text{vc}} = 0.955$ (shape A), 0.932 (B), 0.911 (C), 0.871 (D), 0.925 (E) and 0.866 (F).

*2.2.1. Orientation averaging.* The orientation averaging of optical properties is done by rotating the particle over the three Euler angles ($\alpha_e$, $\beta_e$, $\gamma_e$). Definition of the Euler angles is adapted from Yurkin and Hoekstra (2008). Averaging over $\alpha_e$ is done within a single ADDA computation because rotation over $\alpha_e$ is equivalent to the rotation of the scattering plane. The average over $32\,\alpha_e$ is calculated. Individual ADDA computations are necessary for averaging over $\beta_e$ and $\gamma_e$. For particles with size parameters $x_v < 15$ ($x_v > 15$) averaging over $\beta_e$ is done with a step width of $9°$ ($15°$), and for each $\beta_e$ up to 40 (24) $\gamma_e$ are used for averaging. In summary, for a single particle 526 (206) individual ADDA computations are performed and, if we consider averaging over $\alpha_e$, 16 832 (6592) orientations are evaluated.

*2.2.2. Extension for larger size parameters x.* Only volume-equivalent size parameters $x_v \leq 20.8$ are covered by our ADDA calculations. This range, however, does not cover the complete size spectrum of mineral dust aerosols at our lidar wavelengths. Thus, extensions are required for large particles; we use spheroids for cross-section-equivalent size parameters $x > 20.8$ (this approach is labelled as $\mathcal{X}_{\text{spheroids}}$). Compared to the explicit modelling of the irregularly shaped particles for $x > 20.8$, the utilization of large spheroids will not have any notable effect on extinction, as $C_{\text{geo}}$ is not changed (we use $r = r_c$). However, it may have considerable effects on the lidar ratio $S$ and the linear depolarization ratio $\delta_l$ because these parameters strongly depend on particle shape.

Therefore, as an alternative approach for this extension, we model lidar ratios $S$ and linear depolarization ratios $\delta_l$ of mineral dust ensembles with the assumption that $S$ and $\delta_l$ of single particles are size-independent for cross-section-equivalent size parameters $x \geq 20.8$ (this approach is labelled as $\mathcal{X}_{\text{size}-\text{indep.}}$). A justification of this approach is given in the next section.

*2.2.3. Accuracy.* Inaccuracies of the calculated optical properties of single particles may originate directly from inaccuracies of the ADDA calculations or from orientation averaging. Accuracy tests are performed for shapes B and C (Fig. 1), for four size parameters from 10 to 17.3, and for refractive index $m = 1.52 + 0.0043i$, that is, eight cases are considered.

First, we compare modelled orientation-averaged optical properties with those using more accurate, but more time consuming, settings of ADDA. Using a more accurate stopping criterion for the iterative solver, that is, $10^{-4}$ instead of $10^{-3}$, has only negligible influence on optical properties ($<0.1\%$). Using a grid density of 16 dipoles per wavelength, instead of 11, the extinction efficiency $q_{\text{ext}}$ is found to vary by less than 0.3%, and maximum relative changes of the lidar ratio $S$ and the linear depolarization ratio $\delta_l$ are 1.7% and 2.3%, respectively.

As an additional test, the reciprocity of light scattering (van de Hulst, 1981) is investigated: We compared the modelled intensity at $\theta = 90°$ in a single azimuth direction for a single particle orientation with the modelled intensity for the reversed path of light. The relative difference between corresponding intensities is smaller than 1.3% for all eight cases.

To test the accuracy of the orientation averaging scheme we calculate, for comparison, optical properties using a smaller step width of $5°$ for $\beta_e$ and $\gamma_e$ in the orientation averaging scheme. We find maximum deviations of 0.5% for the extinction efficiency $q_{\text{ext}}$. The relative changes of the lidar ratio $S$ and the linear depolarization ratio $\delta_l$ are smaller than 5% for size parameters $x_v < 15$, and for $x_v = 17.3$ the relative changes are smaller than 8%. It is concluded that orientation averaging is the largest source of error for modelling the optical properties of our irregularly shaped particles.

### 2.3. Optical modelling of spheroids

Besides optical modelling of irregularly shaped particles, which is the main intend of this paper, we also model optical properties of spheroids because they are commonly assumed for non-spherical aerosol particles. For optical modelling of single randomly oriented spheroids we use the extended-precision version of a T-matrix code (Mishchenko and Travis, 1998). Orientation averaging of the optical properties is done analytically by the T-matrix code. Information about the scattering matrix $\mathbf{F}(\theta)$ is calculated in terms of expansion coefficients (Mishchenko and Travis, 1998), which allow the calculation of $\mathbf{F}$ at any scattering angle $\theta$. The maximum size parameter $x$ that can be handled by the T-matrix code depends on the particle shape and the refractive index $m$ (Wiegner et al., 2009). We supplement the T-matrix method calculations with calculations using the geometric optics approach for particles that are not covered by the T-matrix code, that is, $x > 120$ for low $\epsilon'$ and about $x > 25$ for $\epsilon' = 3$. For that, we use a combination of a conventional geometric optics code by Macke and Mishchenko (1996) and an improved geometric optics code by Yang and Liou (1997): The extinction efficiency $q_{\text{ext}}$ and the scattering efficiency $q_{\text{sca}}$ from Yang's code are used, whereas the scattering matrix $\mathbf{F}(\theta)$ is from Macke's code. $\mathbf{F}$ is calculated for 571 scattering angles $\theta$. The T-matrix method is an exact method, whereas the geometric optics approach is an approximate method.

The optical properties of a large number of spheroids is stored in a database (Gasteiger et al., 2011), analogously to the database for irregularly shaped particles (see Sect. 2.2).

## 3. Optical properties of single dust particles

In this section, we discuss lidar-relevant optical properties of single particles. They are illustrated in Fig. 2 for particles of different shapes as a function of the cross-section-equivalent size parameter $x$. The colours and line types are indicated in Fig. 2d. Dotted lines denote undisturbed spheroids with three aspect ratios $\epsilon'$. The same spheroids, but with surface deformations applied (shapes A, B and C), are plotted by solid lines. The
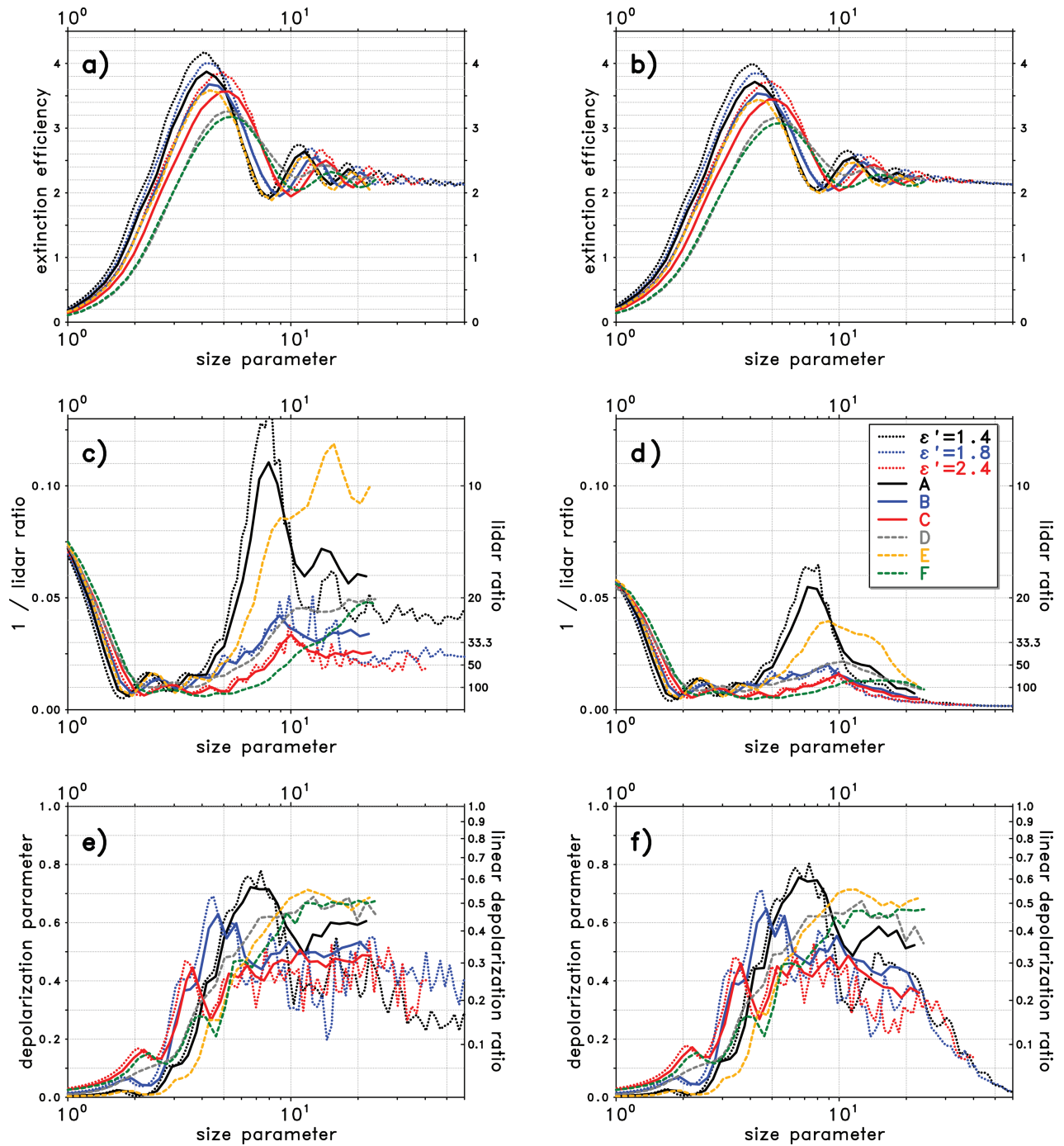
*Fig 2.* Lidar-relevant optical properties over cross-section-equivalent size parameter *x* for single irregularly shaped particles (Fig. 1) and for single prolate spheroids with different aspect ratios $\epsilon'$; left-hand side: non-absorbing particles ($m = 1.52 + 0.0i$), right-hand side: absorbing particles ($m = 1.52 + 0.0172i$).

other shapes (D, E and F) are plotted by dashed lines. Note, that size parameter $x = 10$ corresponds to radii of 0.56 $\mu$m, 0.85 $\mu$m, 1.13 $\mu$m and 1.69 $\mu$m, at the wavelengths of our lidar systems, that is, 355 nm, 532 nm, 710 nm and 1064 nm, respectively. Properties of non-absorbing particles with $m = 1.52 + 0.0i$ (left-hand

side) and absorbing particles with $m = 1.52 + 0.0172i$ (right-hand side) are shown in Fig. 2. These *m* were selected from our scattering database and they are close to the *m* of the mineral dust particles in our reference ensemble of the subsequent sections.

## 3.1. Extinction

The extinction cross section $C_{ext}$ is the most fundamental parameter for the interaction of light with a particle because it is proportional to the amount of light interacting with a particle (comprising absorption and scattering). As a consequence, $C_{ext}$ is relevant for the calculation of all optical properties of aerosol ensembles (e.g. eqs 6, 9 and 11). The extinction efficiency $q_{ext}$, which is the ratio of the extinction cross section $C_{ext}$ and the geometrical cross section $C_{geo}$ of a particle, is shown in Figs. 2a and b. Comparison of $q_{ext}$ of non-absorbing (Fig. 2a) and absorbing (Fig. 2b) particles reveals that absorption has only limited influence on $q_{ext}$, mainly reducing the amplitude of the oscillations. The extinction efficiency $q_{ext}$ at small size parameters ($x < 5$) is shape-dependent, that is, light extinction for given $C_{geo}$ decreases with increasing non-sphericity. Furthermore, the maximum of the extinction efficiency $q_{ext}$ decreases and is shifted towards larger size parameters. With increasing $x$, $q_{ext}$ approaches to a value of 2 for all particles shapes (geometric optics limit). The $q_{ext}$ of large irregularly shaped particles ($x > 10$), after averaging over the oscillations, are slightly smaller than $q_{ext}$ of corresponding spheroids, probably due to weaker edge effects (van de Hulst, 1981).

## 3.2. Lidar ratio S

Figures 2c and d show lidar ratios $S$ as a function of the size parameter. We selected the inverse of the lidar ratio $1/S$ as the vertical coordinate in these figures because the backscattering by a particle is proportional to the term ($C_{ext} \times 1/S$). Consequently, this term is used for the calculation of the backscatter coefficient $\beta$ (eq. 9) and the lidar ratio $S$ of a particle ensemble (eq. 10). As a simple example, we point out that the lidar ratio $S$ of an ensemble of two particles with same $C_{ext}$, but different $S$ of 30 sr and 150 sr, respectively, is 50 sr.

Particles with size parameters $x < 4$ are not effective backscatterers because the extinction efficiency $q_{ext}$ is small for $x < 2$ and $1/S$ is small for $2 < x < 4$. For particles with sizes comparable to the wavelength ($4 < x < 10$) the shape dependence of the lidar ratio $S$ is primarily an aspect-ratio dependence: backscattering strongly increases with decreasing aspect ratio $\epsilon'$. In this size range, surface deformations have only minor influence, which can be seen by comparing deformed spheroids (solid lines) with undisturbed spheroids (dotted lines, same colours). Backscattering by aggregate particles (shape D) is also comparable to backscattering by spheroids with comparable aspect ratio ($\epsilon' = 1.8$). Backscattering by edged particles (shapes E and F) in the range $4 < x < 10$ is also strongly $\epsilon'$-dependent: backscattering by a non-absorbing particle of shape E and size parameter $x \approx 8$ is almost five times as strong as backscattering by the corresponding particle of shape F (compare green with orange dashed lines in Fig. 2c).

For size parameters $x > 10$, backscattering is still aspect-ratio-dependent, but it is also sensitive to the other shape features: Spheroids with surface deformations exhibit slightly stronger backscattering than corresponding spheroids without deformations. Backscattering by aggregate particles (shape D) is clearly enhanced compared to backscattering by corresponding spheroids ($\epsilon' = 1.8$). This difference increases with size: backscattering by aggregate particles with size parameter $x \approx 20$ is about twice as strong as backscattering by corresponding spheroids. At this size parameter, backscattering by non-absorbing particles of shape E, which has the lowest aspect ratio $\epsilon'$, is significantly stronger than backscattering by the other model particle shapes. In summary, the aspect-ratio dependence of the backscattering for $x > 4$ indicates that the lidar ratio $S$ of a mineral dust ensemble is very sensitive to the amount of particles with low aspect ratios $\epsilon'$.

The size dependence of the lidar ratio $S$ of non-absorbing particles (Fig. 2c) with large size parameters ($x > 15$) is small, whereas $S$ becomes very high with increasing $x$ in the case of absorbing particles (Fig. 2d). Backscattering by a two-particle mixture, consisting of an absorbing and the corresponding non-absorbing particle (same shape, size and $m_r$), is clearly dominated by the non-absorbing particle. This means that the size dependence of the lidar ratio $S$ for such two-particle mixtures is also small for large size parameters. As a consequence, the assumption about size-independent $S$ ($\mathcal{X}_{size-indep.}$) for large particles ($x > 20.8$) is not unrealistic for mixtures of absorbing and non-absorbing particles which are modelled in the subsequent sections.

## 3.3. Linear depolarization ratio $\delta_l$

Depolarization parameters $d$ for different particle shapes are shown in Figs. 2e and f. Here, we selected the depolarization parameter $d$ as the vertical coordinate because the product ($C_{ext} \times 1/S \times d/2$) is the relevant parameter for the calculation of the linear depolarization ratio $\delta_l$ of aerosol ensembles (eq. 11). As a simple example, we mention that the depolarization parameter $d$ of an ensemble of two particles with same $C_{ext}$ and $S$, but different depolarization parameters of $d = 0$ (non-depolarizing) and $d = 1$ (fully depolarizing) is $d = 0.5$, whereas the linear depolarization ratio is only $\delta_l = 0.333$. The relation between the depolarization parameter $d$ and the linear depolarization ratio $\delta_l$ is given by eq. (13).

The depolarization parameter $d$ of small particles ($x < 2$) is low and primarily depends on the aspect ratio $\epsilon'$. The depolarization parameter $d$ is hardly sensitive to surface deformations for $x < 10$ (compare solid with dotted lines). For spheroids with aspect ratio $\epsilon' = 1.4$ and $\epsilon' = 1.8$, $d$ has maxima at $x \approx 5$ and $x \approx 7$, respectively. Opposite to this, $d$ of particles with shapes D, E and F increases almost monotonically with particle size up to $x \approx 10$. For comparisons, depolarization parameters $d$ of other model particle shapes are available from other studies:

*Table 1.* Microphysical properties of model aerosol ensembles; properties of reference ensemble are underlined; see text for details.

| Parameter | Label | Cases |
|---|---|---|
| shape of dust | $\mathcal{A}$ | 1: ABCDEF, 2: <u>BCDF</u>, 3: DF, 4: spheroids Dubovik, 5: spheroids Kandler, 6: spheres |
| real refr. index $m_r$ of dust | $\mathcal{B}$ | 1: 1.48, 2: <u>1.53</u>, 3: 1.58 |
| imag. refr. index $m_i$ of dust | $\mathcal{C}$ | 1: $\lambda$-dep. $m_i$ from OPAC, 2: $\lambda$-indep. $m_i = 0.004$ (Table 4) |
| $m_i$-distribution of dust | $\mathcal{D}$ | 1: homogeneous, 2: 1/3 non-absorbing, 3: <u>1/2 non-absorbing</u> |
| size distribution of dust | $\mathcal{E}$ | changed according to Tabs. 2, 3 |
| number of WASO particles | $\mathcal{F}$ | 1: 0, 2: 5, 3: <u>10</u> |
| rel. hum. (relevant f. WASO) | $\mathcal{G}$ | 1: 0%, 2: <u>50%</u> |

The depolarization parameters $d$ of Gaussian spheres ($\sigma = 0.2$), modelled by Lindqvist et al. (2009) for $x = 3$ to $x = 6$, are comparable to $d$ of our shape A. Zubko et al. (2007) investigated the influence of surface roughness on Gaussian spheres. They found that thick-layer roughness reduces $d$ up to $x_{cs} = 12$ [$x_{cs}$ is defined by Zubko et al. (2007) as the size parameter of a circumscribing sphere; our definition of $x$ is estimated to result in 30–40% smaller $x$]. The type of particle roughness by Zubko et al. (2007) is substantially different from the surface deformations of our model shapes, so that the reduction of $d$ due to the roughness is not in contradiction to the insensitivity of $d$ to surface deformations of our shapes A, B and C (for $x < 10$).

Surface deformations are relevant for the depolarization parameter $d$ of large spheroids ($x > 10$): $d$ of spheroids with surface deformations is, on average, about 0.1 higher than $d$ of corresponding particles without surface deformations. For size parameters $x > 10$, the depolarization parameter $d$ of particles of shapes D, E and F is in the range of 0.6–0.7, which corresponds to linear depolarization ratios $\delta_l$ close to 0.5. For the other particle shapes, $d$ is smaller with values in the range of 0.3–0.6, corresponding to $\delta_l$ between 0.2 and 0.4. Ishimoto et al. (2010) modelled particles on which the so-called 'spatial Poisson–Voronoi tessellation' was applied. They modelled the depolarization parameter $d$ for two volume-equivalent size parameters $x_v$, and found $d \approx 0.74$ for $x_v = 14.8$ and $d \approx 0.62$ for $x_v = 24.7$. These values are comparable to the values for our shapes D, E and F. The size dependence of the depolarization parameter of large non-absorbing particles is small (see Fig. 2e), which supports the validity of the assumption of size-independent depolarization for large particles ($\mathcal{X}_{size-indep.}$).

The depolarization parameter of shapes E and F are comparable for size parameters $x > 4$, though their aspect ratios $\epsilon'$ and lidar ratios $S$ are quite different. Furthermore, the depolarization parameters $d$ of large spheroids ($x > 10$) are comparable for different aspect ratios ($\epsilon' = 1.4$, 1.8 and 2.4). This suggests that the aspect ratios $\epsilon'$ of large particles are not the primarily relevant parameters for their depolarization properties. Edges, surface roughness, concave structures and, probably, the overall shape, also influence the depolarization by large particles.

# 4. Optical properties of mineral dust ensembles

This section is devoted to modelling the lidar ratios $S$ and the linear depolarization ratios $\delta_l$ of different mineral dust aerosol ensembles at the wavelengths of our lidar systems (355 nm, 532 nm, 710 nm and 1064 nm). Spectral changes of the extinction coefficient and the backscatter coefficient, expressed by the Ångström exponents $\kappa_{ext}$ and $\kappa_{bsc}$, are also modelled. The single particle properties, discussed in the previous section, provide the basis for the calculation of the ensemble properties. After describing the microphysical properties of the model aerosol ensembles, we study the sensitivity of the optical properties to changes of the microphysical properties of the ensembles.

## 4.1. Microphysical properties of model ensembles

The model ensembles are mixtures of one water-soluble component and three mineral dust components, as proposed by Hess et al. (1998) for the OPAC desert aerosol type. The microphysical properties of the ensembles are described by combining the parameters given in Table 1. For each microphysical parameter (labelled as $\mathcal{A}$–$\mathcal{G}$) two or more cases are considered. For our study, only the relative amount of particles in each of the four components is relevant because we only model intensive optical properties. We specify the number of particles in each of the four components such that the total number of particles in the three mineral dust components in always equal to 1.

The first component of the model ensembles is the water-soluble (WASO) component which consists of small moderately absorbing spherical particles. The size distribution and the refractive index $m$ of the WASO particles depend on the relative humidity, due to their hygroscopicity; their properties are changed in accordance with OPAC (Table 2). In our study, two cases for the relative humidity are modelled (labelled as $\mathcal{G}$, Table 1), that is, 0% and 50%. We consider three cases for the number of WASO particles (labelled as $\mathcal{F}$), namely 0, 5 and 10. Note, that the inclusion of a WASO component is consistent with in situ observations of small volatile particles during the SAMUM-1 campaign (Kandler et al., 2009; Weinzierl et al., 2009).

*Table 2.* Modal radii $r_0$ and width $\sigma$ of log-normal size distributions of components; adapted from Hess et al. (1998).

|        | WASO | MINM | MIAM | MICM |
|--------|------|------|------|------|
| $r_0$ [$\mu$m] | 0.0212 (0% r.h.) | 0.07 | 0.39 | 1.90 |
|        | 0.0262 (50% r.h.) |      |      |      |
| $\sigma$ | 2.24 | 1.95 | 2.00 | 2.15 |

*Table 3.* Number of particles in dust components; total number of dust particles is always equal to 1; properties of reference aerosol ensemble are underlined.

| Label | MINM | MIAM | MICM |
|-------|------|------|------|
| $\mathcal{E}1$ | 0.933 | 0.0671 | 0.000108 |
| $\mathcal{E}2$ | 0.917 | 0.0827 | 0.000226 |
| $\mathcal{E}3$ | 0.898 | 0.1016 | 0.000473 |
| $\mathcal{E}4$ | 0.875 | 0.1242 | 0.000987 |
| $\mathcal{E}5$ | 0.847 | 0.1508 | 0.002045 |

The other three components of the aerosol ensembles are mineral dust components in different size ranges, that is, the nucleation mode (MINM), the accumulation mode (MIAM) and the coarse mode (MICM). The modal radii $r_0$ and the widths $\sigma$ of the log-normal size distributions (eq. 5) of the components are given by OPAC and are independent of the relative humidity. For convenience, the numbers are given in Table 2. For our sensitivity study, the number of particles $N_0$ in the mineral dust modes (label $\mathcal{E}$) are changed as given in Table 3. The resultant size distributions are plotted in Fig. 3 as distributions of particle cross section. The number of large particles increases from $\mathcal{E}1$ to $\mathcal{E}5$, implying an increase of the average size of the dust particles (see MICM in Table 3). The numbers for $\mathcal{E}1$ to $\mathcal{E}5$ were derived from correlations given by Koepke et al. (1997) for particle number densities of 75 cm$^{-3}$, 150 cm$^{-3}$, 300 cm$^{-3}$,
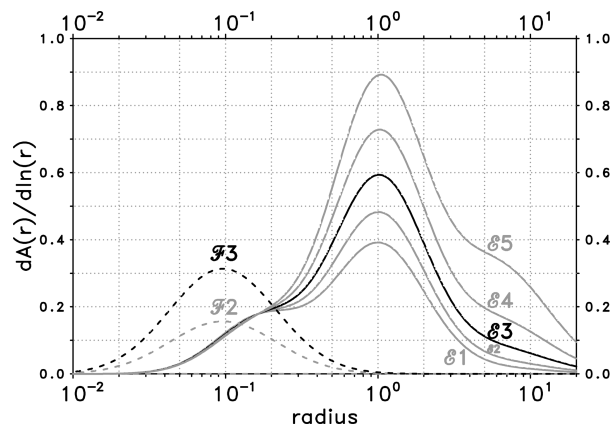


*Fig 3.* Cross-section area distributions of model ensembles (arbitrary scale); solid lines: sum of dust components ($\mathcal{E}$, Table 3); dashed lines: WASO component ($\mathcal{F}$) at 50% r.h.

*Table 4.* Imaginary part of refractive index $m_i$ of particles in dust components at the lidar wavelengths; properties of reference aerosol ensemble are underlined.

| Label | 355 nm | 532 nm | 710 nm | 1064 nm |
|-------|--------|--------|--------|---------|
| $\mathcal{C}1$ | 0.0166 | 0.0063 | 0.0040 | 0.0043 |
| $\mathcal{C}2$ | 0.0040 | 0.0040 | 0.0040 | 0.0040 |

600 cm$^{-3}$ and 1200 cm$^{-3}$, respectively. Note, that this correlation was successfully applied for the interpretation of aerosol optical thickness measurements by Sun photometers during SAMUM-1 (Toledano et al., 2009).

The refractive index $m$ of mineral dust particles is adapted from OPAC. The imaginary part $m_i$ at our lidar wavelengths is given in Table 4 and strongly increases with decreasing wavelength. To study the sensitivity to $m$, the real part $m_r$ is varied by $\pm0.05$ (labelled as $\mathcal{B}$), and an additional case with a wavelength-independent imaginary part $m_i = 0.004$ (labelled as $\mathcal{C}2$) is considered. At short wavelengths, the $m_i$ of case $\mathcal{C}2$ is significantly smaller than the $m_i$ from OPAC ($\mathcal{C}1$), whereas at long wavelengths, they do not differ much. All dust particles in an ensemble have the same real part $m_r$ (as given by $\mathcal{B}$), but we allow distributions of the imaginary part $m_i$ around the average of $m_i$ as given by $\mathcal{C}$. Our study covers three relative distributions of the imaginary part $m_i$ of the dust particles (labelled as $\mathcal{D}$). Very often in optical modelling, $m_i$ is assumed to be the same for all model particles; this is our first case for the relative $m_i$-distribution ($\mathcal{D}1$, homogeneous mixture). In the other cases ($\mathcal{D}2$ and $\mathcal{D}3$, inhomogeneous mixtures), absorbing and non-absorbing dust particles are mixed. The $m_i$ of the absorbing particles is selected such that the average $m_i$ is the same as for the homogeneous mixture. In case $\mathcal{D}2$ one-third of the dust particles are non-absorbing ($m_i = 0$) and two-thirds are absorbing particles with an $m_i$ that is 50% higher than given by $\mathcal{C}$; in case $\mathcal{D}3$ one half of the dust particles are non-absorbing and the $m_i$ of the other dust particles is doubled compared to the $m_i$ given by $\mathcal{C}$. The refractive indices $m$ and the $m_i$-distributions of the dust components are size-independent.

The mineral dust particles are non-spherical. For the dust particle shape (labelled as $\mathcal{A}$) we consider different combinations of irregularly shaped particles (Fig. 1). In the first case ($\mathcal{A}1$) all six particle shapes have equal abundance. In case $\mathcal{A}2$ the particles with low aspect ratio $\epsilon'$ (shapes A and E) are removed from the ensembles, and in case $\mathcal{A}3$ only the most 'extreme' shapes (D and F) are present in the ensembles. In cases $\mathcal{A}1$, $\mathcal{A}2$ and $\mathcal{A}3$, optical properties of prolate spheroids with the $\epsilon'$-distribution from Kandler et al. (2009) are used for $x > 20.8$ ($\mathcal{X}_{\text{spheroids}}$). As an alternative approach, we assume that $S$ and $\delta_l$ are size-independent for $x \geq 20.8$ ($\mathcal{X}_{\text{size-indep.}}$). For comparison, also ensembles of spheroids with the $\epsilon'$-distributions from Dubovik et al. (2006) ($\mathcal{A}4$) and Kandler et al. (2009) ($\mathcal{A}5$), and ensembles of spheres ($\mathcal{A}6$) are modelled.

*Table 5.* Modelled optical properties for different $m_i$-distributions: from SAMUM-1 ('S1'), from SAMUM-2 ('S2'), homogeneous $m_i$($\mathcal{D}1$), 1/3 non-absorbing ($\mathcal{D}2$), 1/2 non-absorbing ($\mathcal{D}3$); other microphysical parameters are the same as in the reference ensemble, except the particle shape, for which $\mathcal{A}5$ is assumed.

|  | S1 | S2 | $\mathcal{D}1$ | $\mathcal{D}2$ | $\mathcal{D}3$ |
|---|---|---|---|---|---|
| $S_{355}$ [sr] | 54 | 43 | 79 | 52 | 43 |
| $S_{532}$ [sr] | 37 | 33 | 43 | 38 | 36 |
| $\omega_{0,355}$ | 0.833 | 0.871 | 0.773 | 0.823 | 0.854 |
| $\omega_{0,532}$ | 0.910 | 0.928 | 0.877 | 0.894 | 0.906 |

### 4.2. Reference aerosol ensemble

As reference ensemble for the sensitivity study, we select an ensemble with optical properties that are consistent with those measured by lidar during SAMUM-1 on 19 May 2006 in Ouarzazate, Morocco (see next section). Measurements from 19 May 2006 were selected because of favourable aerosol conditions. A multitude of measurement platforms were operated on that day, providing the basis for extensive consistency checks (e.g. Müller et al., 2010).

The relative humidity is 50% in the reference ensemble ($\mathcal{G}2$), and the number of WASO particles is 10 ($\mathcal{F}3$); note, that 6.67 WASO particles were proposed in the OPAC desert mixture. The average refractive index $m$ ($\mathcal{B}2$ and $\mathcal{C}1$), as well as the number of particles in the mineral dust modes ($\mathcal{E}3$) is adapted from the OPAC desert mixture. Absorbing and non-absorbing dust particles are mixed with equal abundance ($\mathcal{D}3$), and we assume a mixture of shapes B, C, D and F, each having equal abundance ($\mathcal{A}2$).

The selection of the $m_i$-distribution ($\mathcal{D}$) is critical for the wavelength dependence of the lidar ratio $S$. Therefore, we investigate this aspect by considering $m_i$-distributions from electron-microscopical single particle analysis: Aerosol particles were collected at a ground-based station in Tinfou, Morocco, during SAMUM-1, and at a ground-based station on the airport of Praia, Cape Verde, during SAMUM-2. Using energy-dispersive X-ray spectroscopy, the chemical composition, and from that, the refractive index $m$ of each collected particle was investigated (Kandler et al., 2009, 2011). Thus, refractive index distributions could be obtained for the samples. We utilize $m_i$-distributions of particles with $r > 0.25\,\mu m$ from SAMUM-1 (S1) and SAMUM-2 (S2) as a test of the validity of our $m_i$-distributions ($\mathcal{D}$). We use the same microphysical parameters as for the reference ensemble, but the $m_i$-distribution is exchanged by the distributions from the single particle analysis. Furthermore, spheroids with the aspect ratio distribution from SAMUM-1 (Kandler et al., 2009) are assumed ($\mathcal{A}5$), instead of irregularly shaped particles. Optical parameters that are strongly sensitive to the $m_i$-distribution, that is, the lidar ratio $S$ and the single scattering albedo $\omega_0$, are modelled and given in Table 5.

Optical properties of homogeneous dust mixtures ($\mathcal{D}1$) at 355 nm significantly deviate from the properties of mixtures that consider $m_i$-distributions from SAMUM-1 and SAMUM-2 (S1 and S2), though all mixtures have the same average $m_i$. The lidar ratio $S$ of the homogeneous mixture ($\mathcal{D}1$) at 355 nm is almost twice as high as for the S2 mixture; significant discrepancies are also found for the absorption ($1 - \omega_0$). Mixtures of absorbing and non-absorbing particles ($\mathcal{D}2$ and $\mathcal{D}3$) result in much better agreement with S1 and S2. The lidar ratio $S$ of mixture $\mathcal{D}3$ at 355 nm is equal to the lidar ratio of S2; at 532 nm the difference is only 3 sr, showing that the idealized mixture of 50% absorbing and 50% non-absorbing particles is a reasonable approximation of the $m_i$-distribution of mineral dust particles during SAMUM.

Lidar measurements suggest that the wavelength dependence of the lidar ratio $S$ is small (Tesche et al., 2009). Compared to the homogeneous mixture ($\mathcal{D}1$), mixtures of absorbing and non-absorbing particles ($\mathcal{D}2$ and $\mathcal{D}3$) notably improve the agreement with this finding. Inhomogeneities within mineral dust particles (e.g. Scheuvens et al., 2011) may also be relevant for the wavelength dependence of the lidar ratio $S$, but they are beyond the scope of our study.

### 4.3. Lidar ratio S

Table 6 shows modelled lidar-relevant optical properties of selected aerosol ensembles. Single scattering albedos $\omega_0$ at 355 nm and 532 nm are also given because $\omega_0$ is an important parameter for the radiative transfer. Columns in Table 6 denote different aerosol ensembles, starting with the reference ensemble, followed by modifications of the reference ensemble (labelled with the modified microphysical parameter). Italic numbers in Table 6 denote results assuming size independence of $S$ and $\delta_l$ for large irregularly shaped particles ($\mathcal{X}_{size-indep.}$).

Modelled lidar ratios $S$ at 532 nm over $S$ at 355 nm for all ensembles described in Table 1, except combinations $\mathcal{C}2\,\mathcal{D}2$ and $\mathcal{C}2\,\mathcal{D}3$, are plotted in Fig. 4a, whereas Fig. 4b illustrates $S$ at 710 nm and 1064 nm. The $S$ for irregular-shaped particles (cases $\mathcal{A}1$, $\mathcal{A}2$ and $\mathcal{A}3$) are plotted for assumption $\mathcal{X}_{size-indep.}$. Blue crosses mark results for homogeneous mixtures with $m_i$ from OPAC ($\mathcal{C}1\,\mathcal{D}1$), whereas green ($\mathcal{C}1\,\mathcal{D}2$) and red ($\mathcal{C}1\,\mathcal{D}3$) crosses denote mixtures of absorbing and non-absorbing particles. Results for homogeneous mixtures with wavelength-independent $m_i$ ($\mathcal{C}2\,\mathcal{D}1$) are marked as grey crosses. Consequently, for each colour, all combinations of the other parameters ($\mathcal{A}$, $\mathcal{B}$, $\mathcal{E}$, $\mathcal{F}$ and $\mathcal{G}$) as given in Table 1 are plotted. The properties of the reference ensemble are marked by grey cross hairs.

The lidar ratio $S$ of the reference ensemble is 54 sr at 355 nm, 48 sr at 532 nm, 47 sr at 710 nm and 53 sr at 1064 nm, having a minimum at 710 nm. From Fig. 4a it is immediately clear that the imaginary part of the refractive index $m_i$ and its distribution within the ensembles is relevant for the lidar ratio $S$ at short wavelengths (compare different colours). For example, $S$ of the reference ensemble at 355 nm increases from 54 sr to 83 sr

*Table 6.* Modelled optical properties of selected dust aerosol ensembles; reference ensemble ('Ref.', i.e. combination $\mathcal{A}2\,\mathcal{B}2\,\mathcal{C}1\,\mathcal{D}3\,\mathcal{E}3\,\mathcal{F}3\,\mathcal{G}2$), and variations of reference ensemble (denoted with the varied parameter); italic numbers: results for assumption of size-independent $S$ and $\delta_l$ for $x \geq 20.8$ ($\mathcal{X}_{\text{size-indep.}}$).

| | Ref. | $\mathcal{A}1$ | $\mathcal{A}3$ | $\mathcal{A}4$ | $\mathcal{A}5$ | $\mathcal{A}6$ | $\mathcal{B}1$ | $\mathcal{D}1$ | $\mathcal{C}2\,\mathcal{D}1$ | $\mathcal{E}5$ | $\mathcal{F}1$ | $\mathcal{G}1$ |
|---|---|---|---|---|---|---|---|---|---|---|---|---|
| $S_{355}$ [sr] | 52 | 44 | 50 | 51 | 43 | 24 | 63 | 96 | 55 | 46 | 50 | 48 |
| | *54* | *42* | *49* | | | | *62* | *83* | *46* | *52* | *53* | *50* |
| $S_{532}$ [sr] | 48 | 38 | 46 | 44 | 36 | 18 | 59 | 60 | 53 | 45 | 47 | 46 |
| | *48* | *36* | *44* | | | | *57* | *53* | *47* | *45* | *46* | *46* |
| $S_{710}$ [sr] | 47 | 36 | 46 | 42 | 33 | 15 | 59 | 53 | 53 | 45 | 47 | 47 |
| | *47* | *35* | *44* | | | | *56* | *49* | *49* | *44* | *46* | *46* |
| $S_{1064}$ [sr] | 53 | 40 | 53 | 46 | 35 | 16 | 66 | 58 | 57 | 50 | 53 | 53 |
| | *53* | *39* | *50* | | | | *64* | *55* | *54* | *49* | *53* | *53* |
| $\delta_{l,355}$ | 0.194 | 0.229 | 0.217 | 0.203 | 0.202 | 0.000 | 0.193 | 0.173 | 0.231 | 0.185 | 0.250 | 0.193 |
| | *0.275* | *0.319* | *0.327* | | | | *0.272* | *0.207* | *0.294* | *0.317* | *0.369* | *0.275* |
| $\delta_{l,532}$ | 0.245 | 0.289 | 0.279 | 0.236 | 0.250 | 0.000 | 0.245 | 0.259 | 0.264 | 0.234 | 0.287 | 0.250 |
| | *0.306* | *0.349* | *0.359* | | | | *0.305* | *0.295* | *0.307* | *0.341* | *0.362* | *0.312* |
| $\delta_{l,710}$ | 0.264 | 0.308 | 0.299 | 0.253 | 0.272 | 0.000 | 0.261 | 0.275 | 0.275 | 0.254 | 0.296 | 0.270 |
| | *0.311* | *0.354* | *0.362* | | | | *0.309* | *0.307* | *0.307* | *0.344* | *0.350* | *0.319* |
| $\delta_{l,1064}$ | 0.265 | 0.305 | 0.293 | 0.263 | 0.282 | 0.000 | 0.256 | 0.272 | 0.272 | 0.262 | 0.285 | 0.271 |
| | *0.298* | *0.337* | *0.339* | | | | *0.290* | *0.294* | *0.295* | *0.331* | *0.321* | *0.305* |
| $\kappa_{\text{ext},355-532}$ | 0.244 | 0.243 | 0.253 | 0.211 | 0.210 | 0.210 | 0.248 | 0.244 | 0.248 | 0.126 | 0.033 | 0.184 |
| $\kappa_{\text{ext},532-1064}$ | 0.216 | 0.207 | 0.242 | 0.171 | 0.155 | 0.146 | 0.237 | 0.216 | 0.217 | 0.109 | 0.070 | 0.167 |
| $\kappa_{\text{bsc},355-532}$ | 0.06 | −0.13 | 0.06 | −0.17 | −0.25 | −0.55 | 0.07 | −0.90 | 0.16 | 0.03 | −0.14 | 0.11 |
| | *−0.06* | *−0.17* | *−0.02* | | | | *0.01* | *−0.88* | *0.30* | *−0.20* | *−0.29* | *−0.01* |
| $\kappa_{\text{bsc},532-1064}$ | 0.36 | 0.29 | 0.43 | 0.22 | 0.11 | 0.03 | 0.39 | 0.17 | 0.33 | 0.27 | 0.27 | 0.37 |
| | *0.36* | *0.32* | *0.45* | | | | *0.41* | *0.26* | *0.41* | *0.23* | *0.26* | *0.36* |
| $\omega_{0,355}$ | 0.859 | 0.857 | 0.862 | 0.858 | 0.854 | 0.852 | 0.859 | 0.781 | 0.895 | 0.836 | 0.826 | 0.847 |
| $\omega_{0,532}$ | 0.911 | 0.910 | 0.914 | 0.910 | 0.906 | 0.904 | 0.912 | 0.883 | 0.912 | 0.890 | 0.900 | 0.906 |

(Table 6), if the mixture of absorbing and non-absorbing particles ($\mathcal{D}3$, red) is replaced by the corresponding homogeneous mixture ($\mathcal{D}1$, blue) with the same average refractive index $m$. Interestingly, lidar ratios $S$ of homogeneous ensembles with wavelength-independent $m_i$ (grey) do not significantly deviate from $S$ of the much more realistic mixture of absorbing and non-absorbing particles with wavelength-dependent $m_i$ (red). This suggests that effects due to assuming unrealistic homogeneous absorption properties could partly be compensated by assuming unrealistic wavelength independence of the refractive index $m$. The discrepancy of $S$ at 355 nm between measurements and modelling for homogeneous dust ensembles with wavelength-dependent $m_i$ (e.g. Wiegner et al., 2009; Müller et al., 2010) might be related to the above findings. The sensitivity of $S$ to changes of the $m_i$-distribution decreases with wavelength. Consequently, in Fig. 4b the different colours are not clearly separated.

Furthermore, Table 6 illustrates that the lidar ratio $S$ is also quite sensitive to the particle shape ($\mathcal{A}$) and to the real part of the refractive index $m_r$ ($\mathcal{B}$). These sensitivities are the main reasons for the wide spread of crosses of same colour in Figs. 4a and b, and are consistent with findings from Wiegner et al. (2009). A decrease of $m_r$ by 0.05 ($\mathcal{B}1$) increases $S$ by about 10 sr. Spherical dust particles ($\mathcal{A}6$) reduce $S$ by about 55–70%. A significant size dependence of $S$ was found for homogeneous ensembles in Wiegner et al. (2009), whereas the size dependence of $S$ is only in the order of 2 sr to 4 sr for mixtures of absorbing and non-absorbing particles (compare column $\mathcal{E}5$ with Ref.).

In the previous section we found that backscattering by particles with low aspect ratios ($\epsilon' \leq 1.4$) is significantly stronger than backscattering by particles with larger $\epsilon'$. The presence of particles with small $\epsilon'$ also affects lidar ratios $S$ of ensembles, which can be seen by comparing the reference ensemble with an ensemble in which particles with low $\epsilon'$ are included ($\mathcal{A}1$): $S$ decrease by about 10 sr, if shapes A and E are included. Similar differences are found between spheroids with the $\epsilon'$-distribution from Dubovik ($\mathcal{A}4$, only few particles with $\epsilon' \leq 1.4$) and the $\epsilon'$-distribution from Kandler ($\mathcal{A}5$, many particles with $\epsilon' \leq 1.4$).
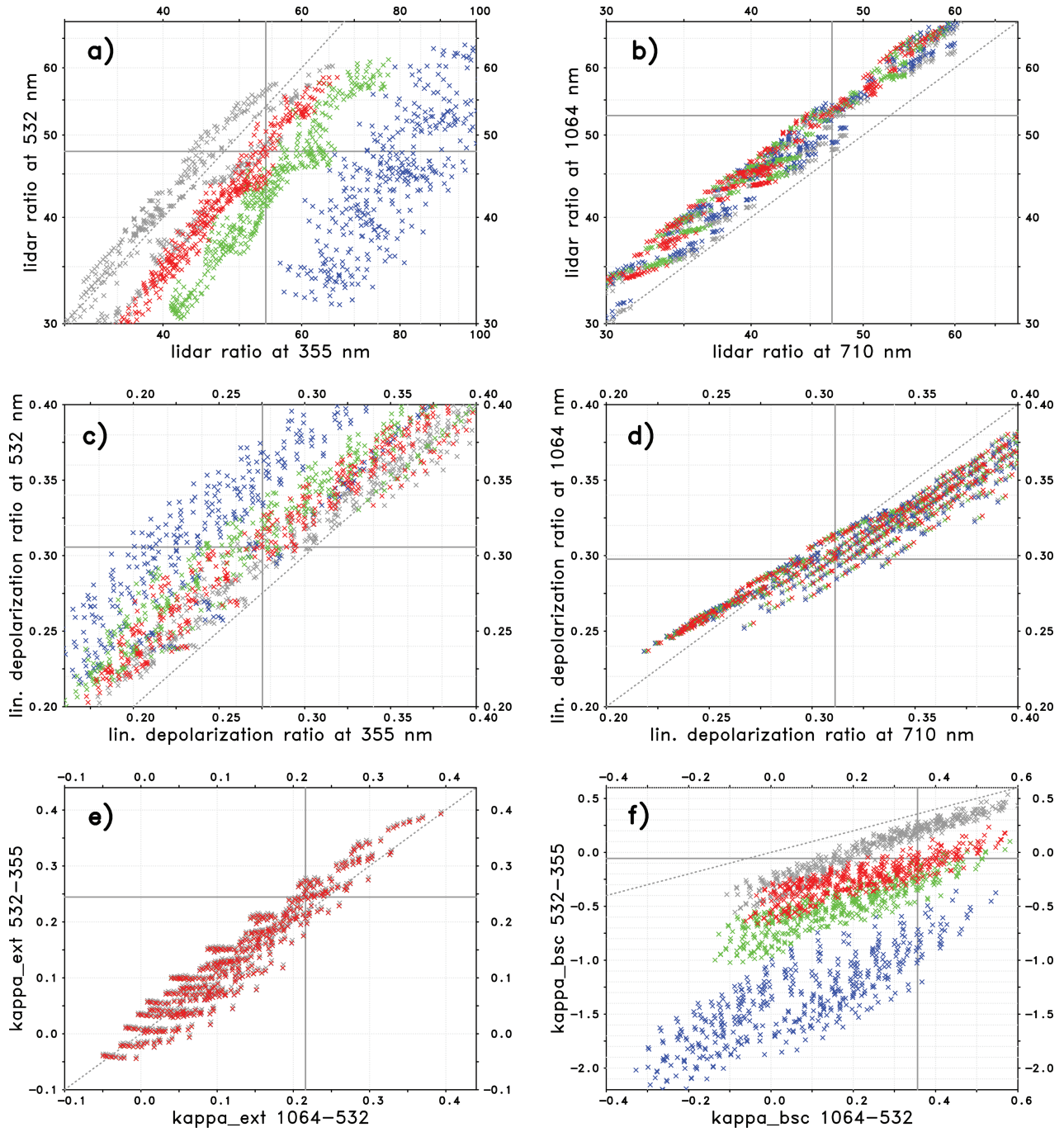
**Fig 4.** Modelled lidar-relevant optical properties of all aerosol ensembles described in Table 1, except combinations $\mathcal{C}2\mathcal{D}2$ and $\mathcal{C}2\mathcal{D}3$; grey cross hairs: reference ensemble; blue: homogeneous ensembles with $m_i$ from OPAC ($\mathcal{C}1\mathcal{D}1$); green and red: ensembles of absorbing and non-absorbing particles with average $m_i$ from OPAC (green: $\mathcal{C}1\mathcal{D}2$; red: $\mathcal{C}1\mathcal{D}3$); grey crosses: homogeneous ensembles with λ-independent $m_i$ ($\mathcal{C}2\mathcal{D}1$); grey dashed lines: λ-independent optical properties.

Comparisons with SAMUM measurements (Tesche et al., 2009) reveal that $S$ for $\mathcal{A}1$ and $\mathcal{A}5$ are too small for an agreement with the measurements (see next section for details). This suggests that the amount of particles with low $\epsilon'$ has to be small for realistic modelling of mineral dust aerosols.

### 4.4. Linear depolarization ratio $\delta_l$

Modelled linear depolarization ratios $\delta_l$ are plotted in Figs. 4c and d for the same wavelength combinations as the lidar ratios $S$ in Figs. 4a and b. Again, size-independent $S$ and $\delta_l$ for large

irregularly shaped particles are assumed ($\mathcal{X}_{\text{size-indep.}}$). The linear depolarization ratio $\delta_l$ of the reference ensemble at 355 nm is 0.275. If we assume spheroids for the large particles ($\mathcal{X}_{\text{spheroids}}$), $\delta_l$ is notably lower ($\delta_l = 0.194$), demonstrating the relevance of large particles for $\delta_l$ of the ensemble at this wavelength. Though we are confident that the assumption of size-independence for $x > 20.8$ ($\mathcal{X}_{\text{size-indep.}}$) is not unrealistic, this fact highlights the need for accurate numerical methods for optical modelling of irregularly shaped particles with large size parameters $x$. In most cases, $\delta_l$ at 355 nm is lower than $\delta_l$ at 532 nm (Fig. 4c), except in cases without WASO particles ($\mathcal{F}$1). We find linear depolarization ratios $\delta_l$ of 0.306 at 532 nm, 0.311 at 710 nm and 0.298 at 1064 nm for the reference aerosol ensemble. Thus, $\delta_l$ of the reference ensemble has a maximum at 710 nm. Two counteracting effects, that is, the low depolarization at small size parameters ($x < 3$, see Fig. 2e) and the presence of WASO particles, give rise to this maximum. If spheroids are assumed at large size parameters ($\mathcal{X}_{\text{spheroids}}$), the maximum of $\delta_l$ is shifted to larger $\lambda$, that is, $\delta_l$ does not decrease from 710 nm to 1064 nm.

The linear depolarization ratio $\delta_l$ is sensitive to most of the microphysical aerosol parameters. First, $\delta_l$ is sensitive to the particle shape ($\mathcal{A}$). Spheroid ensembles ($\mathcal{A}$4 and $\mathcal{A}$5) have lower $\delta_l$ than ensembles of irregularly shaped particles (for $\mathcal{X}_{\text{size-indep.}}$). Sphere ensembles ($\mathcal{A}$6) do not depolarize. Only weak dependence of $\delta_l$ on the real part of the refractive index $m_r$($\mathcal{B}$) is found for irregularly shaped particles. In contrast to that, $\delta_l$ is $m_r$-dependent for spheroids ($\mathcal{A}$4, $\mathcal{A}$5); for example, for $\mathcal{A}$5, $\delta_l$ at 532 nm increases from 0.250 to 0.280, if $m_r$ is reduced from 1.53 to 1.48 ($\mathcal{A}$5 $\mathcal{B}$1, not shown). This is consistent with findings from Wiegner et al. (2009), and indicates that the $m_r$-dependence of $\delta_l$ is a specific feature of spheroids. Homogeneous mixtures with $m_i$ from OPAC ($\mathcal{C}$1 $\mathcal{D}$1, blue) exhibit reduced $\delta_l$ at 355 nm, compared to the other ensembles (see Fig. 4c). Furthermore, we find that the linear depolarization ratio $\delta_l$ is sensitive to the dust size distribution ($\mathcal{E}$), as it increases with increasing amount of large particles. For example, if $\mathcal{E}$5 is applied on the reference ensemble, $\delta_l$ at 532 nm increases from 0.306 to 0.341. The number of WASO particles ($\mathcal{F}$) is also relevant for $\delta_l$, particularly at short wavelengths. With decreasing number of WASO particles, $\delta_l$ increases. For example, by removing the WASO particles from the reference ensemble, $\delta_l$ at 355 nm increases from 0.275 to 0.369. Reducing the relative humidity from 50% to 0% ($\mathcal{G}$1) slightly increases $\delta_l$ at long wavelengths, for example, $\delta_l$ increases by 0.007 at 1064 nm.

### 4.5. Ångström exponent $\kappa_{\text{ext}}$ for extinction

In Fig. 4e modelled Ångström exponents $\kappa_{\text{ext}}$ for the wavelength range from 355 nm to 532 nm are plotted over $\kappa_{\text{ext}}$ for the wavelength range from 532 nm to 1064 nm. $\kappa_{\text{ext}}$ is not sensitive to the $m_i$-distribution (red crosses are above blue and green crosses).

We find that $\kappa_{\text{ext}}$ hardly depends on the wavelength range (cross are close to diagonal). For the reference ensemble

we find $\kappa_{\text{ext}} = 0.244$ for the range from 355 nm to 532 nm and $\kappa_{\text{ext}} = 0.216$ for the range from 532 nm to 1064 nm. The Ångström exponent $\kappa_{\text{ext}}$ mainly depends on the size distribution of dust and WASO particle ($\mathcal{E}$, $\mathcal{F}$ and $\mathcal{G}$). With decreasing contribution of small particles (MINM or WASO), $\kappa_{\text{ext}}$ decreases. For example, $\kappa_{\text{ext}}$ for the range from 355 nm to 532 nm decreases from 0.244 to 0.033, if WASO particles are removed from the reference ensemble. The shape of the dust particles is also relevant, particularly at longer wavelengths. $\kappa_{\text{ext}}$ for the range from 532 nm to 1064 nm is about 0.04–0.07 lower for dust spheroids and spheres ($\mathcal{A}$4, $\mathcal{A}$5 and $\mathcal{A}$6) than for the irregularly shaped particles of the reference ensemble.

### 4.6. Ångström exponent $\kappa_{\text{bsc}}$ for backscatter

In Fig. 4f modelled backscatter-related Ångström exponents $\kappa_{\text{bsc}}$ are shown for the same wavelength ranges as for $\kappa_{\text{ext}}$ in Fig. 4e. Basically, this figure combines information from Figs. 4a, b and e, because $\kappa_{\text{bsc}}$ is a function of $\kappa_{\text{ext}}$ and the wavelength dependence of the lidar ratio $S$ (eqs. 10, 14 and 15). For the reference ensemble we find $\kappa_{\text{bsc}} = -0.06$ for the range from 355 nm to 532 nm, which implies that the backscatter coefficient is virtually the same for 355 nm and 532 nm. If we replace the mixture of absorbing and non-absorbing particles ($\mathcal{D}$3, red) by a homogeneous mixture ($\mathcal{D}$1, blue), $\kappa_{\text{bsc}}$ is only $-0.88$, implying 43% stronger backscattering at 532 nm than at 355 nm, which is in contradiction to typical mineral dust lidar measurements (e.g. Tesche et al., 2009). Thus, homogeneous mixtures result in unrealistic wavelength dependence of backscattering, demonstrating the importance of an adequate treatment of the mineralogical inhomogeneity of mineral dust aerosols for modelling lidar-related optical properties. For spheroids and spheres ($\mathcal{A}$4, $\mathcal{A}$5 and $\mathcal{A}$6), $\kappa_{\text{bsc}}$ is also lower ($-0.17$ to $-0.55$) than for the reference ensemble. For the wavelength range from 532 nm to 1064 nm, $\kappa_{\text{bsc}}$ of the reference ensemble is 0.36, thus the backscatter coefficient decreases by about 22% from 532 nm to 1064 nm.

## 5. Comparison with measurements

In three case studies, we compare modelled optical properties with properties derived from lidar measurements during the SAMUM campaigns. We consider measurements of the high spectral resolution lidar (HSRL) of the German Aerospace Center, operated onboard the Falcon aircraft ($S$ at 532 nm, $\delta_l$ at 532 nm and 1064 nm, Esselborn et al., 2009), measurements of the BERTHA lidar of the Leibniz Institute for Tropospheric Research in Leipzig ($\delta_l$ at 710 nm, Tesche et al., 2009; Tesche et al., 2011), and measurements of the MULIS and POLIS lidars of the Meteorological Institute of the LMU Munich ($S$ and $\delta_l$ at 355 nm and 532 nm, Freudenthaler et al., 2009; Groß et al., 2011). Model ensembles from the previous section are considered for the comparisons, assuming $\mathcal{X}_{\text{size-indep.}}$.

### 5.1. 19 May 2006 (SAMUM-1)

A mineral dust aerosol layer was present over Ouarzazate (30.93°N, 6.90°W, 1133 m a.s.l.), Morocco, on 19 May 2006 from ground to about 5 km a.s.l. Lidar- and in situ measurements showed that the layer was well mixed in the vertical; furthermore, lidar- and Sun photometer measurements showed that the aerosol properties remained stable during the day.

In Fig. 5 we compare lidar ratios $S$ and linear depolarization ratios $\delta_l$ of the reference ensemble with data derived from the lidar measurements of 19 May 2006. $S = 50 \pm 5$ sr at 532 nm was derived from HSRL measurements at 11:09 UTC during the overflight of the Falcon aircraft over Ouarzazate (Esselborn et al., 2009). $S$ of our reference ensemble, which is 48 sr at 532 nm, is in good agreement with this measurement. Though direct measurements of the lidar ratio $S$ at the other wavelengths are not available, Tesche et al. (2009) suggest that $S$ of mineral dust aerosols, observed during SAMUM-1, do not show distinct wavelength dependence. The lidar ratio $S$ of our reference ensemble is in agreement with these findings because it is only slightly wavelength-dependent: it decreases by 6 sr from 355 nm to 532 nm, and increases by 5 sr from 710 nm to 1064 nm.

The linear depolarization ratio $\delta_l$ of the mineral dust aerosol of 19 May 2006 was most likely wavelength-dependent, though the uncertainties of the lidar measurements do not exclude a wavelength-independent $\delta_l$ close to 30% (Fig. 5). Neglecting their uncertainties, the lidar measurements suggest an increase of $\delta_l$ from 355 nm to 532 nm, and a slight decrease of $\delta_l$ from 532 nm to 1064 nm. For the reference ensemble we find the same spectral feature. The linear depolarization ratio $\delta_l = 0.275$ of our reference ensemble at 355 nm is slightly higher than the value derived from the POLIS measurement (0.24), but it is well within the uncertainty range of POLIS (0.17–0.31). At 532 nm we find good agreement of the reference ensemble (0.306) with the values derived from the measurements (MULIS: 0.31; HSRL: 0.30).
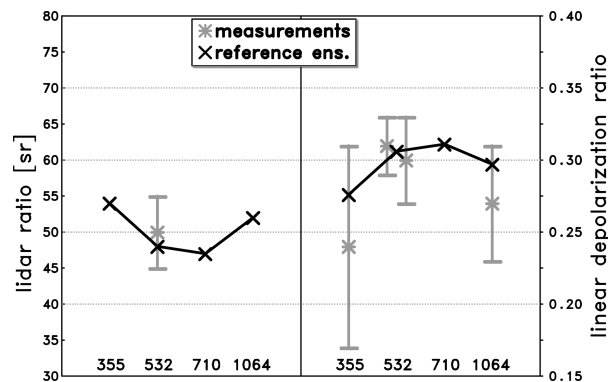
$\delta_l = 0.298$ of the reference ensemble at 1064 nm is also within the uncertainty range of the $\delta_l$ derived from HSRL (0.23–0.31).

Furthermore, it is worthwhile to compare the modelled spectral dependence of the backscattering, expressed by the Ångström exponents for backscatter $\kappa_{bsc}$, with data from lidar. Tesche et al. (2009) found $\kappa_{bsc,355-532}$ of about 0.1 to 0.6 and $\kappa_{bsc,532-1064}$ close to 0.3 from measurements of BERTHA. Measurements of POLIS and MULIS indicate $\kappa_{bsc,355-532}$ close to 0.0 in upper part of the dust layer (not shown). For the reference ensemble we find $\kappa_{bsc,355-532} = -0.06$ and $\kappa_{bsc,532-1064} = 0.36$, which are in the same range as the values from the measurements.

### 5.2. 4 June 2006 (SAMUM-1)

On 4 June 2006 mineral dust aerosols were observed over Ouarzazate in heights up to almost 5 km a.s.l. The extinction coefficient, as measured by the HSRL at 9:47 UTC (Esselborn et al., 2009), was height-dependent with maximum values in heights of 3 km a.s.l. The lidar ratio $S$ varied with height, with values close to 42 sr in a layer from about 2.5 km to 3.5 km a.s.l., and values close to 50 sr above and below this layer. By contrast, the linear depolarization ratio $\delta_l$ was not height-dependent and airborne in situ measurements did not show significant height dependence of the size distribution (Weinzierl et al., 2009).

In Fig. 6 we compare lidar ratios $S$ of the reference ensemble, of an ensemble including particles with low aspect ratios $\epsilon'$ ($\mathcal{A}1$), and an ensemble with an increased real part of the refractive index $m_r$ ($\mathcal{B}3$) with lidar measurements of the aerosol in heights of 2.5–3.5 km a.s.l. Our reference ensemble (48 sr) cannot reproduce the lidar ratio $S$ derived from the HSRL (40 sr to 45 sr at 532 nm). If particles with low $\epsilon'$ are included ($\mathcal{A}1$), the $S$ is only 36 sr, which is lower than the $S$ derived from the HSRL. An increase of $m_r$ of the dust particles from $m_r = 1.53$ (Ref.) to $m_r = 1.58$ ($\mathcal{B}3$) decreases $S$ at 532 nm from 48 sr to 42 sr, resulting in good agreement with the $S$ derived from the



*Fig 5.* Comparison of optical properties of reference ensemble with optical properties from lidar measurements on 19 May 2006 (SAMUM-1).
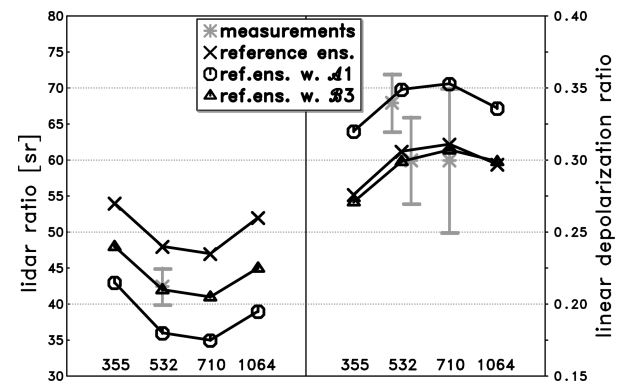


*Fig 6.* Comparison of optical properties of reference ensemble and variations of the reference ensemble with optical properties from lidar measurements on 4 June 2006 (SAMUM-1).

HSRL. Another potential reason for the comparatively low lidar ratios in this dust layer could be changes of the absorption properties of the dust particles (not shown).

For 4 June 2006, linear depolarization ratios $\delta_l$ from measurements are available at 532 nm and 710 nm. $\delta_l = 0.306$ of the reference ensemble at 532 nm is in good agreement with the HSRL measurement (0.27 to 0.33), but slightly lower than values derived from MULIS (0.32 to 0.36) at the same wavelength. At $\lambda = 710$ nm, $\delta_l = 0.311$ of the reference ensemble is in agreement with the values derived from BERTHA (0.25 to 0.35). $\delta_l$ of the ensemble with increased real part of the refractive index $m_r$ ($\mathcal{B}3$) is only slightly lower than $\delta_l$ of the reference ensemble, thus the agreement of both ensembles with the measurements is equally good. For the ensemble including particles with low aspect ratios $\epsilon'$ ($\mathcal{A}1$), $\delta_l$ is notably higher than for the reference ensemble (0.349 versus 0.306 at 532 nm). The agreement of this ensemble with the $\delta_l$ at 532 nm from the MULIS measurements is good, but the same parameter from the HSRL is slightly too low for an agreement with this ensemble. At 710 nm, $\delta_l$ of ensemble $\mathcal{A}1$ (0.353) is close to the upper limit of the uncertainty range of $\delta_l$ derived from BERTHA. A 1:1 mixture of the reference ensemble with the ensemble $\mathcal{A}1$ (Table 6) can reproduce the optical properties ($S$, $\delta_l$) derived from the lidar measurements of 4 June 2006. In this mixture, shapes A and E have a relative abundance of 0.1, and shapes B, C, D and F a relative abundance of 0.2.

### 5.3. 29 January 2008 (SAMUM-2)

In the late evening of 29 January 2008 high aerosol extinction coefficients $\alpha$ were observed by lidar at the airport of Praia (15.94° N, 23.49° W, 75 m a.s.l.), Cape Verde, where the SAMUM-2 field campaign took place. The mineral dust layer extended up to heights of about 1 km above ground. Some differences of the linear depolarization ratio $\delta_l$ between the aerosol below and above 0.5 km were observed, probably due to mixing of small amounts of maritime aerosols into the lower layer. Thus, we use the optical data of the layer from 0.5 km to 0.8 km ($\delta_l$) and 0.6 km to 0.8 km ($S$) (Groß et al., 2011) for the comparison of mineral dust properties with optical modelling results.

From measurements of POLIS and MULIS (overlap heights < 0.4 km), lidar ratios $S$ at 355 nm are available; they are in the range from 60 sr to 66 sr. A lidar ratio $S$ of $63 \pm 2$ sr at 532 nm is derived from MULIS measurements. These $S$ are higher than the $S$ derived from the HSRL during SAMUM-1 (see earlier). The lidar ratio $S$ of the reference ensemble is lower than $S$ derived from the measurements (Fig. 7) . A high lidar ratio $S$ may be modelled by a low real part of the refractive index $m_r$. Figure 7 shows that $S$ at 355 nm is in good agreement with the measurement for $m_r = 1.48$ ($\mathcal{B}1$). At 532 nm, however, $S$ is still slightly lower (57 sr) than the $S$ derived from the measurement; considering the variability of $S$ within the aerosol layer ($\pm 4$ sr,
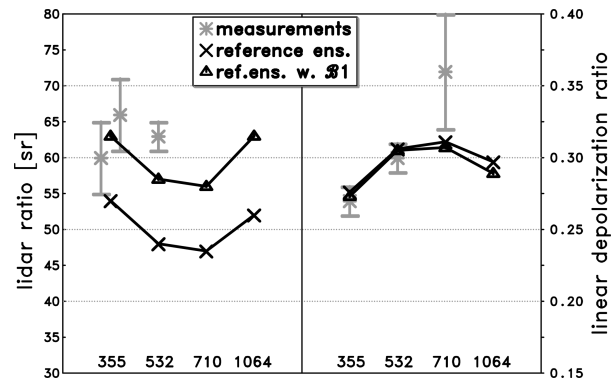


*Fig 7.* Comparison of optical properties of reference ensemble and variations of the reference ensemble with optical properties from lidar measurements on 29 January 2008 (SAMUM-2).

Groß et al., 2011), the lidar ratio of ensemble $\mathcal{B}1$ agrees with the measurements.

During SAMUM-2, higher iron contents compared to SAMUM-1 were present in the aerosols, affecting the absorption properties of the aerosols (Kandler et al., 2011; Müller et al., 2011). The increase of the lidar ratio $S$ from SAMUM-1 to SAMUM-2 may be explained by these higher iron contents or by changes of the mineralogical inhomogeneity of the aerosols, but detailed studies are required for final conclusions.

At 355 nm, the linear depolarization ratio $\delta_l$ of the reference ensemble (0.275) and of the ensemble with $m_r = 1.48$ ($\mathcal{B}1$, 0.272) are in agreement with the POLIS measurement (uncertainty from 0.26 to 0.28). Similarly, at 532 nm, the agreement is good. At 710 nm the modelled $\delta_l$ (0.311 and 0.309, respectively) are only slightly lower than the values derived from BERTHA measurements (0.32–0.40). An increase of $\delta_l$ from 532 nm to 710 nm is a common feature of these models and measurements, though the increase of $\delta_l$ in the models is weaker than in the measurements.

From the MULIS measurements in the same layer, $\kappa_{\text{bsc},355-532} = -0.15$ with an estimated uncertainty of 0.3 is derived (not shown). $\kappa_{\text{bsc},355-532}$ of the reference ensemble ($-0.06$) and ensemble $\mathcal{B}1$ (0.01) is good agreement with the value from the measurement.

## 6. Summary and conclusions

Optical modelling of mineral dust aerosols is challenging because of the complex microphysical properties of natural dust particles. Optical modelling, however, is required for a wide range of applications, for example, for the interpretation of remote sensing and optical in situ measurements, for modelling the radiative transfer in dust clouds, and thus for estimates of climate impacts of dust aerosols. We investigated the optical properties of ensembles of absorbing and non-absorbing irregularly shaped dust particles. These complex model ensembles

improved the representation of the microphysical properties of natural dust aerosols, compared to common models with ensembles of symmetric dust particles, all having the same refractive index $m$. The focus of this study was on lidar remote sensing, for which the backscattering properties of the aerosols are relevant.

As the first step of our study, we investigated lidar-relevant optical properties of single dust particles. We found that backscattering by particles with low aspect ratios ($\epsilon' \leq 1.4$) is significantly stronger than backscattering by particles with high aspect ratios. Surface deformations do hardly affect backscattering and depolarization at size parameters $x < 10$. For larger particles, surface deformations on prolate spheroids moderately strengthen backscattering and depolarization. Large aggregate particles and edged particles show stronger backscattering and depolarization than corresponding spheroids. In general, the size dependence of backscattering and depolarization of large non-absorbing particles is small.

As the next step, we modelled lidar-relevant optical properties of ensembles in which absorbing and non-absorbing irregularly shaped dust particles are mixed to mimic the natural mineralogical inhomogeneity of dust. Wavelength-dependent refractive indices from the OPAC aerosol database are considered. A sensitivity study revealed that the inhomogeneity of the absorption properties strongly affects the lidar ratio at short wavelengths. Interestingly, the lidar ratios are similar to a homogeneous ensemble with wavelength-independent refractive index; this indicates that effects due to common assumptions (homogeneity of $m$ and wavelength independence of $m$) partly compensate each other. Consequently, it can be expected that no agreement with lidar observations is possible for models that only consider the wavelength dependence of $m_i$ but not the inhomogeneity of the absorption properties. For typical dust refractive indices, ensembles of irregularly shaped dust particles, in general, have higher linear depolarization ratios than ensembles of spheroids.

As the final step, we compared modelled lidar-relevant optical properties with properties derived from SAMUM lidar measurements. The comparisons revealed that good agreement is possible: Mixtures of absorbing and non-absorbing particles are essential for realistic wavelength dependence of the lidar ratio. For agreement of the absolute values of lidar ratio, the amount of particles with low aspect ratios ($\epsilon' \leq 1.4$) has to be low. Agreement of the linear depolarization ratio is possible for irregularly shaped dust particles with typical dust refractive indices.

Our study demonstrated that an improved model representation of the microphysical properties of mineral dust aerosols clearly improves the agreement with optical properties from lidar measurements. Further improvements could be expected from a detailed investigation of the effect of the mineralogical inhomogeneity of dust aerosols on the absorption, and from the availability of accurate methods for irregularly shaped particles with very large size parameters. In this respect, the consideration of the size dependence of the refractive index and the particle shape may also be beneficial.

Because of the complexity of microphysical properties of mineral dust aerosols and the inherent large number of unknown parameters, an unambiguous determination of dust microphysical properties is not possible from lidar measurements alone. By using information about the aerosols from independent measurements, the ambiguity might be reduced. A potential source of such information are photometers, which measure direct solar irradiances and sky radiances at several wavelengths. The sensitivity of these optical parameters is different from the sensitivity of lidar-relevant optical parameters. For example, the extinction and the sky radiances in the aureole of the Sun, which can be measured by the photometer, are primarily sensitive to the size of the particles. By synergistic combination of optical data from lidars and photometers, improvements can be expected for the retrieval of microphysical dust properties. Therefore, as a subsequent step, we plan to investigate in detail the sensitivity of multispectral radiances to changes of dust properties.

# 7. Acknowledgments

# References

Ansmann, A., Petzold, A., Kandler, K., Tegen, I., Wendisch, M., and co-authors. 2011. Saharan Mineral Dust Experiments SAMUM-1 and SAMUM-2: what have we learned? *Tellus* **63B**, in press.

Böckmann, C. and Wauer, J. 2001. Algorithms for the inversion of light scattering data from uniform and non-uniform particles. *J. Aerosol Sci.* **32**, 49–61. doi:10.1016/S0021-8502(00)00052-5.

Dubovik, O., Sinyuk, A., Lapyonok, T., Holben, B. N., Mishchenko, M., and co-authors. 2006. Application of spheroid models to account for aerosol particle nonsphericity in remote sensing of desert dust. *J. Geophys. Res.* **111**, D11208. doi:10.1029/2005JD006619.

Esselborn, M., Wirth, M., Fix, A., Weinzierl, B., Rasp, K., and co-authors. 2009. Spatial distribution and optical properties of Saharan dust observed by airborne high spectral resolution lidar during SAMUM 2006. *Tellus* **61B**, 131–143. doi:10.1111/j.1600-0889.2008.00394.x.

Freudenthaler, V., Esselborn, M., Wiegner, M., Heese, B., Tesche, M., and co-authors. 2009. Depolarization ratio profiling at several wavelengths in pure Saharan dust during SAMUM 2006. *Tellus* **61B**, 165–179. doi:10.1111/j.1600-0889.2008.00396.x.

Gardner, G. Y. 1984. Simulation of natural scenes using textured quadric surfaces. In: *Proceedings of the 11th Annual Conference on Computer Graphics and Interactive Techniques.* ACM press, New York, pp. 11–20.

Gasteiger, J., Groß, S., Freudenthaler, V. and Wiegner, M. 2011. Volcanic ash from iceland over munich: mass concentration retrieved from ground-based remote sensing measurements. *Atmos. Chem. Phys.* **11**, 2209–2223. doi:10.5194/acp-11-2209-2011.

Gimmestad, G. G. 2008. Reexamination of depolarization in lidar measurements. *Appl. Opt.* **47**, 3795–3802. doi:10.1364/AO.47.003795.

Groß, S., Tesche, M., Freudenthaler, V., Toledano, C., Wiegner, M., and co-authors. 2011. Characterization of Saharan dust, marine aerosols and mixtures of biomass burning aerosols and dust by means of multi-wavelength depolarization- and Raman-measurements during SAMUM-2. *Tellus* **63B**, in press.

Heintzenberg, J. 2009. The SAMUM-1 experiment over Southern Morocco: overview and introduction. *Tellus* **61B**, 2–11. doi:10.1111/j.1600-0889.2008.00403.x.

Hess, M., Koepke, P. and Schult, I. 1998. Optical Properties of Aerosols and Clouds: The Software Package OPAC. *Bull. Amer. Meteor. Soc.* **79**, 831–844. doi:10.1175/1520-0477(1998)079<0831:OPOAAC>2.0.CO;2.

van de Hulst, H. C. (ed.) 1981. *Light Scattering by Small Particles*, H. C. Dover Publications, New York.

Ishimoto, H., Zaizen, Y., Uchiyama, A., Masuda, K. and Mano, Y. 2010. Shape modeling of mineral dust particles for light-scattering calculations using the spatial Poisson-Voronoi tessellation. *J. Quant. Spectrosc. Radiat. Transfer* **111**, 2434–2443. doi:10.1016/j.jqsrt.2010.06.018.

Kalashnikova, O. V. and Sokolik, I. N. 2004. Modeling the radiative properties of nonspherical soil-derived mineral aerosols. *J. Quant. Spectrosc. Radiat. Transfer* **87**, 137–166. doi:10.1016/j.jqsrt.2003.12.026.

Kandler, K., Schütz, L., Deutscher, C., Ebert, M., Hofmann, H., and co-authors. 2009. Size distribution, mass concentration, chemical and mineralogical composition and derived optical parameters of the boundary layer aerosol at Tinfou, Morocco, during SAMUM 2006. *Tellus* **61B**, 32–50. doi:10.1111/j.1600-0889.2008.00385.x.

Kandler, K., Lieke, K., Benker, N., Emmel, C., Küpper, M., and co-authors. 2011. Electron microscopy of particles collected at Praia, Cape Verde, during the Saharan Mineral dust experiment: particle chemistry, shape, mixing state and complex refractive index. *Tellus* **63B**, doi:10.1111/j.1600-0889.2011.00550.x.

Koepke, P., Hess, M., Schult, I. and Shettle, E. 1997. Global Aerosol Data Set, report No. 243 of the Max-Planck-Institut fuer Meteorologie, Hamburg, Germany.

Lindqvist, H., Muinonen, K. and Nousiainen, T. 2009. Light scattering by coated Gaussian and aggregate particles. *J. Quant. Spectrosc. Radiat. Transfer* **110**, 1398–1410. doi:10.1016/j.jqsrt.2009.01.015.

Macke, A. and Mishchenko, M. I. 1996. Applicability of regular particle shapes in light scattering calculations for atmospheric ice particles. *Appl. Opt.* **35**, 4291–4296. doi:10.1364/AO.35.004291.

Mishchenko, M. I. and Travis, L. D. 1998. Capabilities and limitations of a current Fortran implementation of the T-Matrix method for randomly oriented, rotationally symmetric scatterers. *J. Quant. Spectrosc. Radiat. Transfer* **60**, 309–324. doi:10.1016/S0022-4073(98)00008-9.

Müller, H. and Quenzel, H. 1985. Information content of multispectral lidar measurements with respect to the aerosol size distribution. *Appl. Opt.* **24**, 648–654. doi:10.1364/AO.24.000648.

Müller, D., Wandinger, U. and Ansmann, A. 1999. Microphysical particle parameters from extinction and backscatter lidar data by inversion with regularization: theory. *Appl. Opt.* **38**, 2346–2357. doi:10.1364/AO.38.002346.

Müller, D., Ansmann, A., Freudenthaler, V., Kandler, K., Toledano, C., and co-authors. 2010. Mineral dust observed with AERONET Sun photometer, Raman lidar, and in situ instruments during SAMUM 2006: shape-dependent particle properties. *J. Geophys. Res.* **115**, D11207. doi:10.1029/2009JD012523.

Müller, T., Schaditz, A., Kandler, K. and Wiedensohler, A. 2011. Spectral particle absorption coefficients, single scattering albedos, and imaginary parts of refractive indices from ground based in-situ measurements at Cape Verde Island during SAMUM-2. *Tellus* **63B**, doi:10.1111/j.1600-0889.2011.00572.x.

Nousiainen, T. 2009. Optical modeling of mineral dust particles: a review. *J. Quant. Spectrosc. Radiat. Transfer* **110**, 1261–1279. doi:10.1016/j.jqsrt.2009.03.002.

Osterloh, L., Böckmann, C., Mamouri, R. E. and Papayannis, A. 2011. An adaptive base point algorithm for the retrieval of aerosol microphysical properties. *Open Atmos. Sci. J.* **5**, 61–73. doi:10.2174/1874282301105010061.

Piller, N. B. and Martin, O. J. F. 1998. Increasing the performance of the coupled-dipole approximation: a spectral approach. *IEEE Trans. Antennas Propag.* **46**, 1126–1137. doi:10.1109/8.718567.

Satheesha, S. K. and Moorthy, K. K. 2005. Radiative effects of natural aerosols: a review. *Atmos. Environ.* **39**, 2089–2110. doi:10.1016/j.atmosenv.2004.12.029.

Scheuvens, D., Kandler, K., Küpper, M., Lieke, K., Zorn, S., and co-authors. 2011. Individual-particle analysis of airborne dust samples collected over Morocco in 2006 during SAMUM-1. *Tellus* **63B**, in press.

Sokolik, I. N. and Toon, O. B. 1999. Incorporation of mineralogical composition into models of the radiative properties of mineral aerosol from UV to IR wavelengths. *J. Geophys. Res.* **104**, 9423–9444. doi:10.1029/1998JD200048.

Tesche, M., Ansmann, A., Müller, D., Althausen, D., Mattis, I., and co-authors. 2009. Vertical profiling of Saharan dust with Raman lidars and airborne HSRL in southern Morocco during SAMUM. *Tellus* **61B**, 144–164. doi:10.1111/j.1600-0889.2008.00390.x.

Tesche, M., Groß, S., Ansmann, A., Müller, D., Althausen, D., and co-authors. 2011. Profiling of Saharan dust and biomass burning smoke with multiwavelength polarization Raman lidar at Cape Verde. *Tellus* **63B**, doi:10.1111/j.1600-0889.2011.00548.x.

Toledano, C., Wiegner, M., Garhammer, M., Seefeldner, M., Gasteiger, J., and co-authors. 2009. Spectral aerosol optical depth characterization of desert dust during SAMUM 2006. *Tellus* **61B**, 216–228. doi:10.1111/j.1600-0889.2008.00382.x.

Ulanowski, Z., Bailey, J., Lucas, P. W., Hough, J. H. and Hirst, E. 2007. Alignment of atmospheric mineral dust due to electric field. *Atmos. Chem. Phys.* **7**(24), 6161–6173. doi:10.5194/acp-7-6161-2007.

Valery, A., Cartwright, R., Fausett, E., Ossipov, A., Pasko, E., and co-authors. 1999. HyperFun project: a framework for collaborative multidimensional F-rep modeling. *Eurographics/ACM SIGGRAPH Workshop Implicit Surfaces 99*, Bordeaux, France.

Veselovskii, I., Dubovik, O., Kolgotin, A., Lapyonok, T., Di Girolamo, P., and co-authors. 2010. Application of randomly oriented spheroids for retrieval of dust particle parameters from multiwavelength lidar measurements. *J. Geophys. Res.* **105**, D21203. doi:10.1029/2010JD014139.

Weinzierl, B., Petzold, A., Esselborn, M., Wirth, M., Rasp, K., and co-authors. 2009. Airborne measurements of dust layer properties, particle size distribution and mixing state of Saharan dust during SAMUM 2006. *Tellus* **61B**, 96–117. doi:10.1111/j.1600-0889.2008.00392.x.

Wiegner, M., Gasteiger, J., Kandler, K., Weinzierl, B., Rasp, K., and co-authors. 2009. Numerical simulations of optical properties of Saharan dust aerosols with emphasis on lidar applications. *Tellus* **61B**, 180–194. doi:10.1111/j.1600-0889.2008.00381.x.

Yang, P. and Liou, K. N. 1997. Light scattering by hexagonal ice crystals: solutions by a ray-by-ray integration algorithm. *J. Opt. Soc. Am. A* **14**, 2278–2289. doi:10.1364/JOSAA.14.002278.

Yurkin, M. A. and Hoekstra, A. G. 2008. User manual for the Discrete Diploe Approximation Code ''Amsterdam DDA" (version 0.78.2).

Yurkin, M. A., Maltsev, V. P. and Hoekstra, A. G. 2007. The discrete dipole approximation for simulation of light scattering by particles much larger than the wavelength. *J. Quant. Spectrosc. Radiat. Transf.* **106**, 546–557. doi:10.1016/j.jqsrt.2007.01.033.

Yurkin, M. A., Min, M. and Hoekstra, A. G. 2010. Application of the discrete dipole approximation to very large refractive indices: filtered coupled dipoles revived. *Phys. Rev. E* **82**, 036703. doi:10.1103/PhysRevE.82.036703.

Zubko, E., Muinonen, K., Shkuratov, Y., Videen, G. and Nousiainen, T. 2007. Scattering of light by roughened Gaussian random particles. *J. Quant. Spectrosc. Radiat. Transfer* **106**, 604–615. doi:10.1016/j.jqsrt.2007.01.050.